The International Journal of Advanced Manufacturing Technology (2018) 97:2621–2633
https://doi.org/10.1007/s00170-018-2104-9

ORIGINAL ARTICLE

Residual stress development in selective laser-melted Ti6Al4V: a parametric thermal modelling approach

Haider Ali[1] · Hassan Ghadbeigi[1] · Kamran Mumtaz[1]

Received: 6 February 2018 / Accepted: 3 May 2018 / Published online: 18 May 2018

Abstract

High cooling rates within the selective laser melting (SLM) process can generate large residual stresses within fabricated components. Understanding residual stress development in the process and devising methods for in-situ reduction continues to be a challenge for industrial users of this technology. Computationally efficient FEA models representative of the process dynamics (temperature evolution and associated solidification behaviour) are necessary for understanding the effect of SLM process parameters on the underlying phenomenon of residual stress build-up. The objective of this work is to present a new modelling approach to simulate the temperature distribution during SLM of Ti6Al4V, as well as the resulting melt-pool size, solidification process, associated cooling rates and temperature gradients leading to the residual stress build-up. This work details an isotropic enhanced thermal conductivity model with the SLM laser modelled as a penetrating volumetric heat source. An enhanced laser penetration approach is used to account for heat transfer in the melt-pool due to Marangoni convection. Results show that the developed model was capable of predicting the temperature distribution in the laser/powder interaction zone, solidification behaviour, the associated cooling rates, melt-pool width (with 14.5% error) and melt-pool depth (with 3% error) for SLM Ti6Al4V. The model was capable of predicting the differential solidification behaviour responsible for residual stress build-up in SLM components. The model-predicted trends in cooling rates and temperature gradients for varying SLM parameters correlated with experimentally measured residual stress trends. Thus, the model was capable of accurately predicting the trends in residual stress for varying SLM parameters. This is the first work based on the enhanced penetrating volumetric heat source, combined with an isotropic enhanced thermal conductivity approach. The developed model was validated by comparing FEA melt-pool dimensions with experimental melt-pool dimensions. Secondly, the model was validated by comparing the temperature evolution along the laser scan path with experimentally measured temperatures from published literature.

Keywords Finite element · Cooling rate · Temperature gradient · Selective laser melting · Additive manufacturing · Ti6Al4V · Residual stress

1 Introduction

Additive manufacturing (AM) techniques form three-dimensional components directly from a digital model by joining materials layer by layer [1, 2]. The expanded geometric freedom of the process, low material wastage and rapid product development cycles make these technologies attractive to a variety of industries [2]. The AM process selective laser melting uses a high-power laser to completely melt compositions of metallic feedstock from a powder bed. Due to the rapid heating and cooling cycles of successive layers, large thermal gradients are generated which in turn can create high residual stresses within fabricated components [3]. The process-induced residual stresses may lead to in process part failure due to geometric distortion, built-in cracking or premature failure of parts subjected to alternating loading or corrosive environments [3–9]. The complex nature of the layer-by-layer building process and thermal cycling requires a robust understanding of the numerous physical phenomena associated with the selective laser melting (SLM) process in order to be able to control residual stress and improve the quality of parts [10]. Using sub-optimal SLM processing parameters can lead to build failure or may result in part properties falling below requirement (e.g. low part density) [11]. Practical

✉ Kamran Mumtaz
k.mumtaz@sheffield.ac.uk

[1] Department of Mechanical Engineering, University of Sheffield, Sheffield S1 3JD, UK

experimentation is generally used to determine the optimal manufacturing process parameters for SLM [12–16] and is often supplemented with computer simulations using finite element modelling to increase the understanding of the processing conditions.

Several attempts have been made to model the SLM process [8, 10, 11, 17–35]. Shiomi et al. [21] developed an FE simulation to predict the temperature distribution and the amount of solidified material within metallic powders irradiated by a pulsed laser. The model was validated by comparing the experimentally measured weight of solidified material against model predictions for different combinations of power and exposure time. It was reported that the effect of laser power variations are more effective than the varied exposure time on the maximum temperature reached by metallic powder. Matsumoto et al. [22] proposed an FE method for estimating temperature and stress distribution in a single laser-processed solidified layer. Gusarov et al. [26, 33] developed a coupled radiation and heat transfer model for estimating the thermal distribution within an SLM powder layer. Roberts et al. [32] considered temperature-dependent material properties and phase changes to develop a three-dimensional model of SLM Ti6Al4V. The model was used to predict the thermal and residual stress distribution resulting from layer-by-layer processing approach during SLM using ABAQUS element birth and death method. Song et al. [28] created a three-dimensional FE simulation to predict optimal SLM processing parameters. The model results were validated by building high-density parts with parameters, for which the model had predicted a melt-pool depth of 45 μm using 50-μm powder layer thickness. Correct modelling of the SLM process is a useful tool for control and optimisation of the process [18]. These studies did not consider the heat flow in the melt-pool due to Marangoni convection or heat loss due to vaporisation, since the powder was assumed to be a homogeneous solid section with thermo-physical properties of powder.

Marangoni convection or fluid flow greatly influences the heat transfer within the melt-pool formed by the SLM process [36]. Modelling the SLM process without considering the heat transfer in the melt-pool due to fluid flow can lead to inaccurate (very high) temperature predictions in the range of 14,000 °C reported by Fu et al. [17], for a three-dimensional FE model of SLM Ti6Al4V. Khairallah et al. [11] developed a three-dimensional mesoscopic, multi-physics model, to demonstrate the effect of the stochastic nature of powder distribution in powder bed systems. It was found that surface tension of the melt-pool drives the physics of the process and affects the heat transfer and the topology of solidified melt-pool. Three-dimensional, computational fluid dynamics (CFD) was also used to predict the melt-pool geometry and temperature distribution in SLM by Yuan et al. [37]. The heat transfer due to the fluid flow in the melt-pool was modelled using an enhanced anisotropic thermal conductivity approach by Safdar et al. [18], where the thermal conductivity of the material was adjusted to account for the experienced thermal process. It is reported by Safdar et al. [18] that the geometry and thermal distribution in the melt-pool were predicted accurately without involving the complexity and/or longer processing time involved in using the CFD modelling approach. However, the anisotropic models are expected to be computationally more expensive compared with the case where all the material properties are assumed to be isotropic. Three-dimensional multiple-layer models of SLM were developed by Cheng et al. [38] and Parry et al. [35], where the laser beam was considered as a volumetric heat source with a known penetration into the material to account for the heat flow in the melt-pool. Parry et al. [35] reported temperatures as high as 12,000 °C in the melt-pool and this peak temperature was termed as an isolated singularity above the vaporisation temperature of Ti6Al4V. Understanding the physical phenomenon associated with laser processing of materials and predicting the microstructure of the SLM components depend on the appropriate temperature prediction during the process. This will also provide a more realistic view of the temperature gradients and cooling rates associated with the process which can help in understanding the mechanical properties and residual stress behaviour of SLM components. Lopez et al. [34] recently developed a two-dimensional FE model based on the enhanced anisotropic thermal conductivity approach to simulate the thermal behaviour of SLM AA-2024. The FE model was validated by comparing experimental melt-pool dimensions with model-predicted melt-pool dimensions. The thermal history from the FE model was coupled with cellular automata model for accurately predicting the microstructure of the material and the results were validated experimentally.

Ti6Al4V is light weight and possesses high strength at low to moderate temperatures [39]. It also has excellent corrosion resistance, is biocompatible and has good machinability. It has a wide range of applications within aerospace, automotive and medical sectors and is one of the most commonly processed materials using SLM. Based on this material's extensive usage, this investigation models the melting of Ti6Al4V to understand the thermal behaviour and its effect on residual stress development in SLM components.

Increasing the thermal conductivity enhancement factor leads to increasing computation time, and therefore, the present research proposes a modelling strategy to simulate the SLM process for Ti6Al4V by modelling the laser beam as a volumetric heat source (modelled using ABAQUS DFLUX subroutine), with enhanced penetration depth. The enhanced penetration depth is expected to account for part of the heat flow in the melt-pool and thus require lower thermal conductivity enhancement factors. This is expected to improve the computational efficiency of the FEA model. The proposed model considers temperature-dependent material properties with phase change from powder-liquid-solid (modelled by

ABAQUS USDFLD subroutine). This work also proposes two modelling reduction approaches which will assist in simulating the substrate and the surrounding powder as a heat sink without the requirement to increase the size of the model. Since the surrounding powder and substrate are modelled as boundary conditions the model is independent of the platform size. The proposed model is used to estimate the effect of SLM process parameters on cooling rates and temperature gradients to determine the effect of parametric variations on residual stresses in SLM components.

2 Modelling methodology

The modelling approach used within this work is based upon the concept of a moving volumetric heat source, combined with enhanced thermal conductivity. The melting behaviour of a single line containing 14 laser spots was simulated. A 1.04 × 0.33 mm, powder layer of 50-μm thickness was deposited on a substrate with a thickness of 0.5 mm. A length of 1.04 mm was chosen such that only one laser spot with extra powder is modelled at the beginning and end of laser scan track. A width of 0.325 mm was chosen such that only two laser spots with extra powder is modelled on either side of laser scan track. The choice of small sizes for extra powder to be modelled and the small thickness of the substrate was to illustrate the effectiveness of the modelling reduction approaches. ABAQUS 8-node linear heat transfer brick element (DC3D8) was used for meshing. A mesh size of 32.5 × 32.5 × 50 μm was used for the powder layer. The substrate mesh was biased to move from 50 μm at the top of the model, increasing to 100 μm at the bottom to minimise the number of mesh elements and reduce the computation time. The SLM process uses a localised laser beam to heat and melt feedstock from the powder bed; heat transfer therefore plays an important role in the process. The general, spatial and temporal distribution of the temperature is governed by the heat conduction equation (Eq. (1)).

$$\rho C_p \frac{\partial T}{\partial t} = k_{xx}\frac{\partial^2 T}{dx^2} + k_{yy}\frac{\partial^2 T}{dy^2} + k_{zz}\frac{\partial^2 T}{dz^2} + \dot{q} \tag{1}$$

where T is temperature; t is time; x, y and z are the spatial coordinates; k_{xx}, k_{yy} and k_{zz} are the thermal conductivities; ρ is the density; C_p is the specific heat and $\dot{q}$ is the heat source term.

2.1 Initial conditions

Powder was modelled to be deposited with an initial temperature of 25 °C. Substrate pre-heating was also applied as an initial temperature condition to the substrate. The value of the temperature applied to the substrate was varied according to the parameters being modelled.

2.2 Heat source

Using ABAQUS DFLUX subroutine written in FORTRAN, a moving volumetric heat source was programmed to simulate the laser. The volumetric heat source was used to account for the laser penetration effect into the powder, which according to Fischer et al. [25] is 63 μm for commercially pure titanium powder. In order to make the simulation more efficient, the volumetric heat source was applied to a 50-μm powder layer thickness along with 250-μm depth in substrate. The variation of laser intensity in the radial direction was modelled using a modified cylindrical laser heat flux (MCHF) model as explained in refs. [8, 40].

$$\dot{q}_{\text{mod cyl}} = 0.864\eta\frac{P}{\Pi {r_{\text{las}}}^2} \tag{2}$$

Equation (2) shows the MCHF model, where P is laser power in watts; r_{las} is radius of laser spot on the bed surface, which was taken as 50 μm for the Renishaw AM250 SLM machine, and η is the laser absorptivity value for Ti6Al4V. Absorptivity value of 0.6 was chosen after a few trials with different values around $\eta = 0.77$ [41], for pure titanium.

$$I_{\text{r}} = 2.55 q_{\text{mod cyl}} \tag{3}$$

In Eq. (3), I_{r} is intensity of laser in the radial direction used in this research. The correction factor of 2.55 found through trial and error is necessary for achieving the correct melt-pool size and temperature distribution.

$$I_z = -15z^2 + 4z + 2 \tag{4}$$

Equation (4) shows the variation of laser intensity in the depth direction (Z-axis), modelled as a parabolic relation (see Fig. 1).

$$\dot{q} = (I_r \times I_z) \tag{5}$$

Equation (5) shows the definition of the heat flux used for simulating the moving heat source in this work.

2.3 Material properties

Material phase change was modelled using a user subroutine (USDFLD) in order to predict the powder-liquid-solid phase change based on the temperature of the laser-irradiated region. Temperature-dependent material properties of solid and powder Ti6Al4V used in this research were taken from the work by Roberts [8], except thermal conductivity of powder Ti6Al4V which was taken from the work by Parry et al.

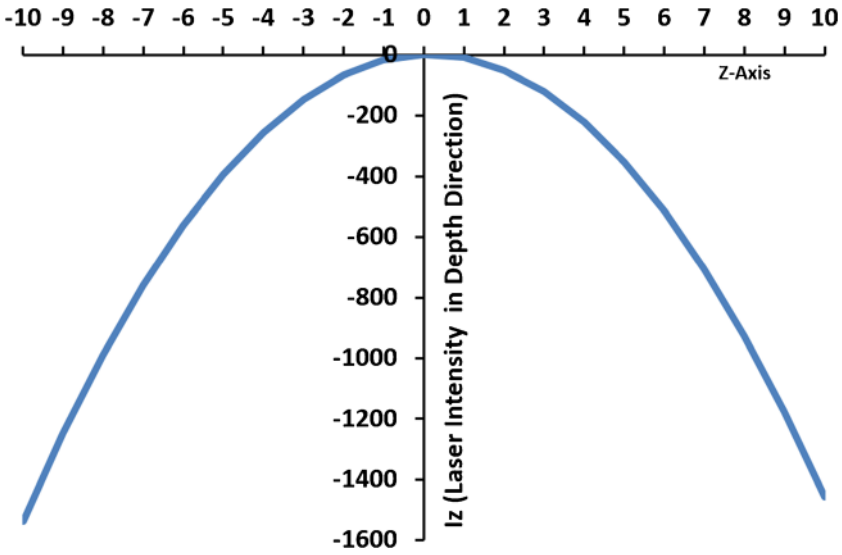

Fig. 1 Laser intensity variation in *Z*-axis

[35]. In order to artificially simulate the Marangoni convection responsible for heat flow in the melt-pool, an enhanced thermal conductivity model presented by Safdar et al. [18] was used but isotropic thermal conductivity was considered instead of anisotropic conductivity [18], as shown in Eq. (6). According to Safdar et al. [18], isotropic enhanced thermal conductivity approach has been used by many researchers to simplify and speed up the modelling process to account for melt-pool convection. Therefore, this work uses the isotropic enhanced thermal conductivity approach to improve the computational efficiency of the FEA model.

$$K' = \Lambda K \tag{6}$$

where K' is the enhanced isotropic thermal conductivity of the melt-pool, K is the normal isotropic thermal conductivity at a given temperature for molten material and Λ is the thermal conductivity enhancement factor, defined by Eq. 7.

$$\Lambda = \begin{cases} 1 & if\ T < T_{melt} \\ Multiplying\ factor & if\ T > T_{melt} \end{cases} \tag{7}$$

An isotropic enhancement factor of $\Lambda = 4.0$ was used in this work, based on trial and error to achieve the desired melt-pool dimensions. Due to the enhanced penetration of the volumetric heat source, the thermal conductivity factor had a more pronounced effect on the width of the melt-pool compared to the depth.

2.4 Heat losses

During the SLM process, the majority of heat is lost through conduction to the substrate and surrounding powder. Heat loss also occurs due to convection and radiation from the top surface during the process. For simplicity, radiation heat losses were not considered in this work and also according to Polivnikova [29], radiation heat losses are negligible. Convective heat loss from the top surface due to flow of inert gas in the chamber was modelled with a convective heat transfer coefficient of $20\frac{W}{m^2-K}$.

In order to simulate the conductive heat loss to the substrate, a surface film condition was defined on the five surfaces of the substrate (Fig. 2a). Temperature-dependent conductivity of solid Ti6Al4V was used as a convective heat transfer coefficient on the selected surfaces.

$$h_1 = k_{\text{solid}}(T) \tag{8}$$

where h_1 is the convective heat transfer coefficient applied on the four sides and bottom of the modelled small substrate to account for the heat losses into actual (larger) substrate and $k_{\text{solid}}(T)$ is the temperature-dependent thermal conductivity of solid Ti6Al4V adapted from the work by Roberts [8].

In order to simulate the conductive heat loss to the surrounding powder, a surface film condition was defined on the four surfaces of the powder layer (see Fig. 2b). Temperature-dependent conductivity of powder Ti6Al4V was used as a convective heat transfer coefficient on the selected surfaces.

$$h_2 = k_{powder}(T) \tag{9}$$

where h_2 is the convective heat transfer coefficient applied on the four sides of the modelled small powder layer to account for the heat losses into surrounding powder and k_{powder} is the temperature-dependent thermal conductivity of powder Ti6Al4V adapted from the work by Parry et al. [35]. These modelling reduction approaches helped in reducing model size and thus computational time.

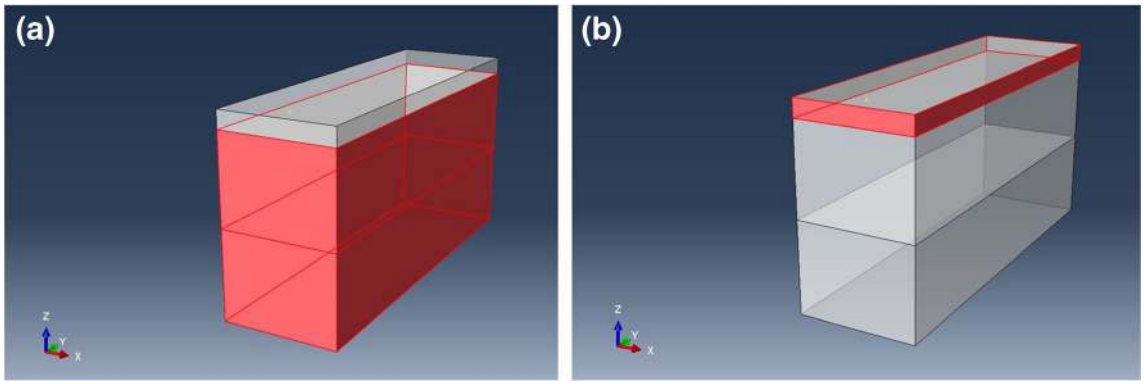

Fig. 2 **a** Surfaces for conduction to substrate. **b** Surfaces for conduction to surrounding powder

3 Experimental methodology

3.1 Thermal model validation

Three 20-mm-long single lines were melted from a 50 μm layer of Ti6Al4V powder deposited onto a titanium substrate using a Renishaw AM250 machine with optimised (> 99% part density) build parameters (details in ref. [12]), for experimental melt-pool measurement. The substrate was cross sectioned, mounted, polished and etched for 20 s with Kroll's reagent to reveal the melt-pool. Using an optical microscope, images of the substrate region with the SLM-melted scan lines were acquired and ImageJ was used to measure the melt-pool dimensions. The simulated melt-pool dimensions were determined by taking a cross-sectional view of the melted line and measuring the melt-pool dimensions. The thermal FEA model was validated by comparing the simulated melt-pool size with experimentally measured values.

3.2 Residual stress measurement

Three 30 × 30 × 10 mm blocks were designed and manufactured to determine the process induced residual stresses. The parts were fabricated using a layer thickness (lt) of 75 μm and parameters (obtained from density optimization trials) shown in Table 1.

Air-abrasive hole drilling using ASTM E837-13a [42] was used to measure residual stress on the top surface of the blocks (depth of 2 mm into the sample), with an average error of 5–20% in residual stress values. This is a semi-destructive method capable of measuring bi-axial normal (σ_{xx}, σ_{yy}) and shear (τ_{xy}) stresses [43].

Using the parameters shown in Table 1, energy density required for nearly fully dense (99.9% dense) SLM Ti6Al4V parts using 75-μm layer thickness was calculated using Eq. (10).

$$E = \frac{P \times t}{\mathrm{pd} \times h \times \mathrm{lt}} \tag{10}$$

The required energy density for 75-μm-layer-thickness SLM Ti6Al4V parts to achieve nearly fully dense parts is $61.5 \frac{J}{\mathrm{mm}^3}$.

3.3 Validation of the effect of FEA-predicted cooling rate on residual stress

Keeping the energy density constant at 61.5 J/mm^3, the power was lowered to 150 W and using Eq. 10, the exposure was calculated to be 160 μs. FEA simulation was used to estimate the cooling rate from a 75-μm single line using the parameters shown in Table 2.

FEA model predicted a lower cooling rate for the combination of parameters shown in Table 2; therefore, three 30 × 30 × 10 mm blocks were manufactured using a layer thickness of 75 μm and parameters shown in Table 2. Residual stress was measured using air-abrasive hole drilling based on ASTM E837-13a [42].

Table 1 Optimised parameters for 75-μm-layer-thickness SLM builds

Power (P), (W)	Exposure (t), (μs)	Point distance (pd), (μm)	Hatch spacing (h), (μm)	Substrate temperature (°C)
200	120	65	80	100

Table 2 SLM Ti6Al4V parameters based on the concept of maintaining energy density constant and varying power and exposure

Power (P), (W)	Exposure (t), (μs)	Point distance (pd), (μm)	Hatch spacing (h), (μm)	Substrate temperature (°C)
150	160	65	80	100

4 Results and discussion

4.1 Validation of thermal modelling

This section presents the model validation approaches taken for this work. Firstly, the model was validated based on comparison of experimentally measured melt-pool dimensions against model-predicted melt-pool dimensions. Secondly, the model was validated based on the trend in temperature evolution history over a scanning length of 325 μm. FEA-predicted temperature distribution in the *XY*-plane along the laser scanning direction was compared with experimentally determined values for SLM of Ti64 by Yadroitsev et al. [44]. The experimental measurement of temperature distribution in the melt-pool was carried out using a single-mode continuous-wave, 1075-nm wavelength, Ytterbium fibre laser with 70-μm spot size [44]. In the study by Yadroitsev et al. [44], melt-pool temperature at the Ti6Al4V substrate without powder was measured at laser powers (*P*) of 20, 30 and 50 W, in combination with scanning speed (*V*) 0.1, 0.2 and 0.3 m/s from ten single tracks of 10-mm length. Temperature distribution in the melt-pool was measured by a specially designed coaxial optical system using a 782 × 582 pixel resolution CCD camera [44].

4.1.1 Melt-pool dimensions

Experimental melt-pool dimensions from three 20-mm-long line sample cross sections were compared with model-predicted melt-pool dimensions. Figure 3 shows a comparison of average experimental melt-pool width (186 μm) and depth (169 μm) against model-predicted melt-pool width (159 μm) and depth (164 μm).

Representative optical micrograph of the experimentally acquired melt-pool with average melt-pool dimensions is shown in Fig. 4a. Experimental melt-pool had an average width of 186 μm and an average depth of 169 μm.

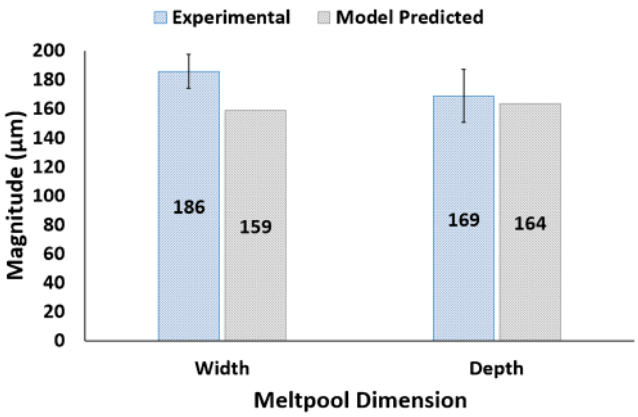

Fig. 3 Experimental and model-predicted melt-pool dimension comparison

Figure 4b shows the melt-pool dimensions predicted from the ABAQUS finite element model, using optimised (> 99% part density) SLM build parameters (details in ref. [12]). The FEA model predicted a melt-pool width of 159 μm. The predicted melt-pool width is 14.5% less than the average experimentally measured melt-pool width of 186 μm. It can be seen from Fig. 4b that the FEA model predicted a melt-pool depth of 164 μm. The predicted melt-pool depth is 3% less than the average experimentally measured depth of 169 μm. Therefore, based on the comparison of melt-pool dimensions shown in Fig. 4, the FEA model prediction of the melting behaviour of Ti6Al4V when irradiated by laser correlates well with experiments. This FEA model was used for studying the parametric dependence of residual stress in SLM Ti6Al4V parts. It was used for estimating the effect that varying SLM process parameters had on cooling rates and temperature gradients within the process.

4.1.2 Melt-pool temperature distribution

The second usage of the FEA model was to estimate the temperature distribution across the melt-pool. Figure 5 shows a comparison of FEA-predicted temperature distribution in the *XY*-plane along the laser scanning direction (points of interest highlighted in sub Fig. 5(b)), with experimentally determined distribution of the brightness temperature for SLM of Ti64 [44], in the *XY*-plane along the laser scanning direction. Figure 5 shows a good correlation of the trend in FEA-predicted temperature distribution with experimentally measured temperature distribution. In the experimentally determined temperature distribution [44], the material's solidification region is highlighted to commence at approximately 220 μm behind the current position of the laser. Figure 5 shows that the FEA model predicted a similar solidification region.

The experimentally determined temperatures are for a solid Ti6Al4V substrate using a laser power of 50 W and scanning velocity of 0.1 m/s [44], while the FEA-predicted temperature distribution is for 50 μm Ti6Al4V powder layer on a solid substrate using a laser power of 200 W and scanning velocity of 0.64 m/s. FEA-predicted temperatures are higher than the experimentally measured values because the experimental temperatures are brightness temperature, and according to Yadroitsev et al. [44–46], the true melt-pool temperature values should be higher. According to Yadroitsev et al. [44–46], the true peak melt-pool temperature for 50-W laser power and 0.1-m/s scanning velocity was calculated to be 2710 K (corresponding brightness temperature being 2340 K). According to refs. [44–46], laser power has a more pronounced effect on the melt-pool peak temperature compared with scan speed (exposure or irradiation time). Yadroitsev et al. [44] experimentally determined the dependence of melt-pool peak temperature on laser power and

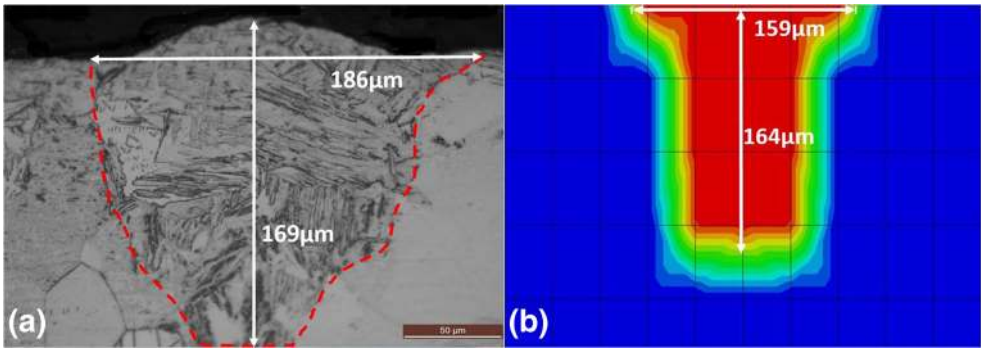

Fig. 4 **a** Experimentally measured melt-pool dimensions. **b** Melt-pool dimensions predicted by ABAQUS finite element thermal model

irradiation time, concluding that the peak temperature of the melt-pool is more sensitive to laser power. Therefore, the model-predicted temperature should have been much higher than the true experimental temperatures as the model uses a much higher power. The reason for not achieving much higher temperatures could probably be attributed to the laser spot size, as the modelled laser spot size (100 µm) is bigger than the experimental laser spot size (70 µm). The results in Fig. 5 show that the trend in model-predicted temperature evolution over the laser scan path agrees well with the trend in experimental trends and therefore will result in accurate predictions of the cooling rate and temperature gradients. The predicted cooling rate and temperature gradients provides insight into the residual stress build-up.

4.2 Temperature distribution and solidification behaviour predicted from FEA

Figure 6a shows the temperature distribution in the *XY*-plane (top view) along the laser scanning direction. It can be seen from Fig. 6a that the melt-pool has an elongated tail surrounded by recently solidified material. The melt-pool is symmetrical around the line the laser centre traverses. Similar melt-pool shapes have been reported by Cheng et al. [24], from FEA model of IN718, and Polivnikova [29] reported similar shape of melt-pool for 18Ni(300) maraging steel using Mathematica software. The material starts solidifying around the edges first with the material in the centre, taking longer to solidify. This variation in temperature between the central molten material and the recently solidified material on the sides creates a temperature gradient and, thus according to the temperature gradient mechanism [40, 47], will result in residual stress build-up in the SLM components. Figure 6b shows a dimensioned isometric view with laser scanning direction and the region used for volumetric heat addition.

Figure 6c illustrates the temperature and material solidification evolution along the depth, *ZY*-plane (front view) of laser scan path along the laser scanning direction. An important feature to note within Fig. 6c is that the melt-pool starts solidifying from the bottom and moves upward. Thus, the analysis of solidification front movement from Fig.6a, c, is used to suggest the movement of solidification front indicated by the

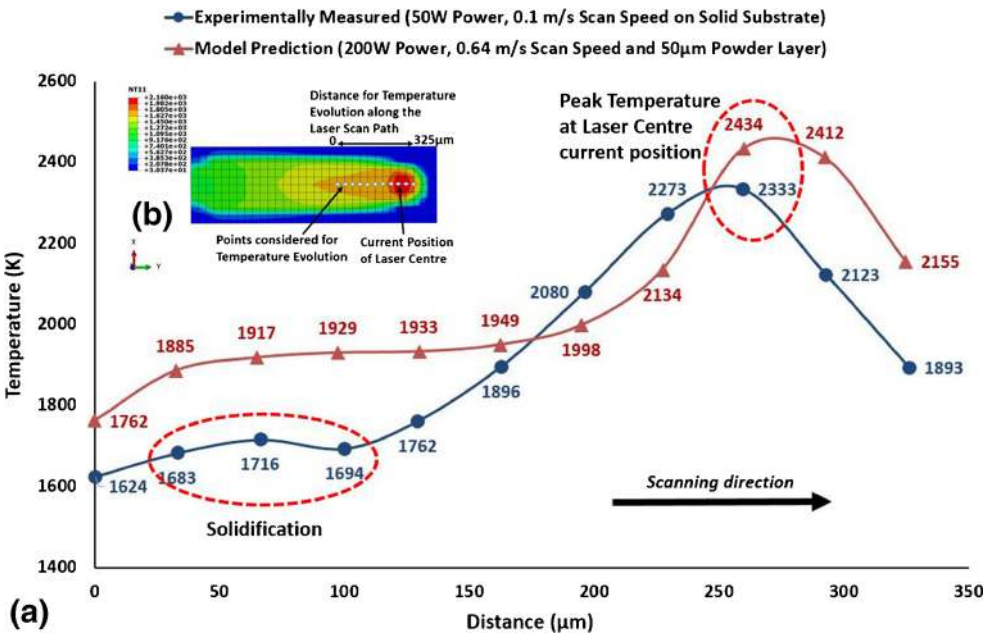

Fig. 5 **a** Comparison of FEA model-predicted temperature in *XY*-plane along the laser scanning direction with experimentally determined distribution of the brightness temperature in the *XY*-plane along the laser scanning direction; $P = 50$ W and $V = 0.1$ m/s values adapted from ref. [44]. (b) The 325-µm distance with points considered for FEA model-predicted temperature in *XY*-plane along the laser scanning direction

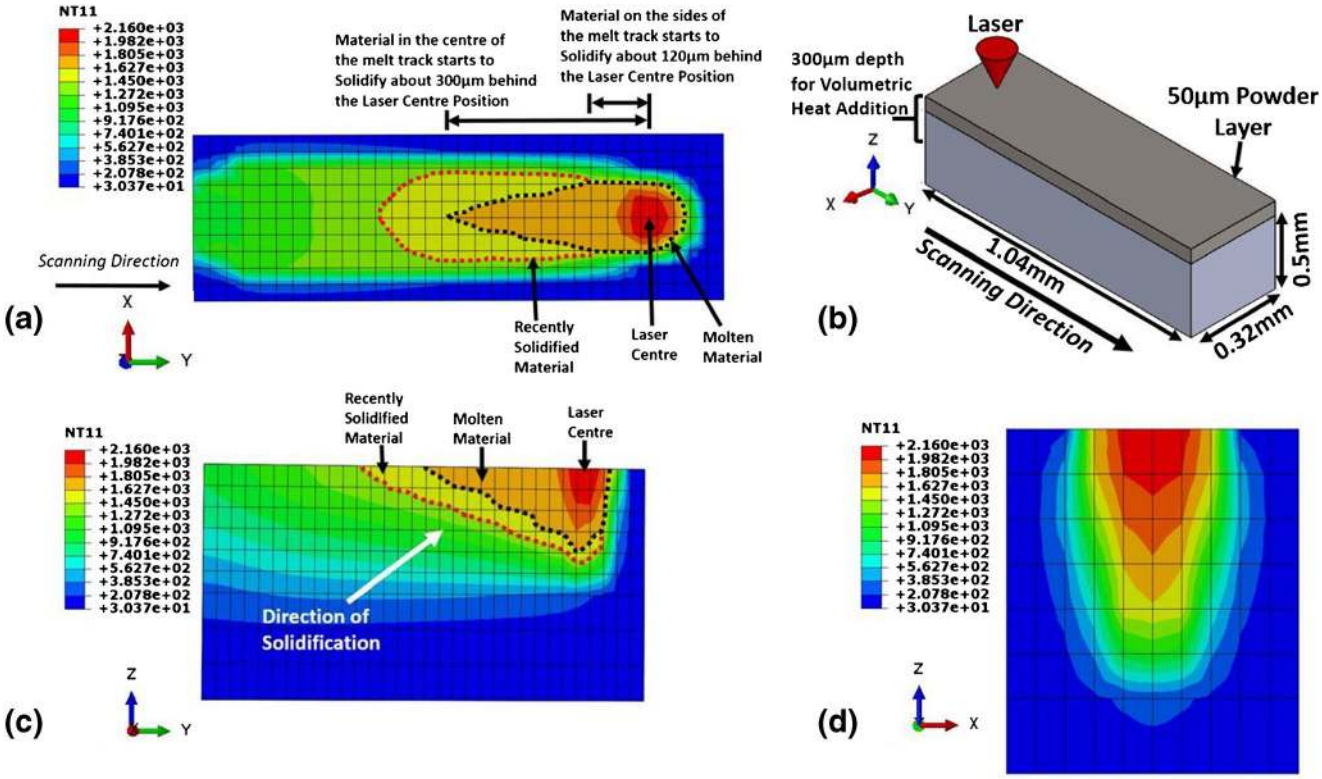

Fig. 6 **a** (top view) Temperature and material solidification evolution along the laser scan path in *XY*-plane along the laser scanning direction. **b** Dimensioned isometric view showing the depth used for volumetric heat addition. **c** (front view) Temperature and material solidification evolution along the depth of laser scan path in *ZY*-plane along the laser scanning direction. **d** (side view) Temperature distribution across the depth (*ZX*-plane of the melt-pool)

white arrow in Fig. 6c. Thus, the underlying solidified material restricts the shrinkage of the molten material on top and, according to the cool-down phase model [47, 48], is responsible for the generation of residual stress in SLM components.

Figure 6d shows the temperature distribution across the depth *ZX*-plane (side view) of the melt-pool. The highest temperature of 2160 °C occurs at the top surface of the melt-pool. The temperature distribution spreads out along the *X*-axis in the substrate region due to higher conductivity of the solid substrate surrounding the melt-pool compared to the powder layer, whereas powder has lower conductivity. It can also be seen from Fig. 6d that the temperature gradient along the depth (*Z*-axis) of the melt-pool increases in the substrate region. This high temperature gradient across the melt-pool depth will result in differential contraction upon cooling and, according to temperature gradient mechanism [40, 47] and cool-down phase model [47, 48], is responsible for the development of residual stress in SLM components.

4.3 Cooling rate and temperature gradient prediction from FEA relationship with experimentally determined residual stress

FEA simulation was used to predict the temperature gradient and cooling rates for SLM Ti6Al4V with samples built at different bed pre-heat temperatures. Figure 7(a) shows that the temperature gradient between the top surface of the melt-pool and 250 µm below the melt-pool top surface (sub Fig. 7(b) highlights the two points in the cross-sectional view of the model) decreases with increasing powder bed pre-heat temperature. According to temperature gradient mechanism [40, 47], a decrease in temperature gradient should result in lowering residual stress and thus an increase in bed pre-heat temperature should also result in a decrease in residual stresses. According to the residual stress results presented by Ali et al. [12] (shown in Fig. 8), increasing powder bed pre-heat temperatures resulted in lowering of residual stress. The trend in temperature gradient for varying bed pre-heat temperatures predicted from the FEA simulation correlates with the residual stress values reported by Ali et al. [12]. According to refs. [4, 8, 48–50], pre-heating is responsible for a reduction in temperature gradients in SLM builds and the FEA simulation predicted the same effect as shown in Fig. 7.

Another interesting observation from Fig. 7 is that the peak temperature in the melt-pool increases with increasing bed pre-heat temperature up to 470 °C while the peak temperature at 570 °C (2073 °C) is even lower than at bed pre-heat temperature of 100 °C (2081 °C). A reason for this drop in melt-pool peak temperature could possibly be related to the start of endothermic microstructural phase transformation at pre-heat

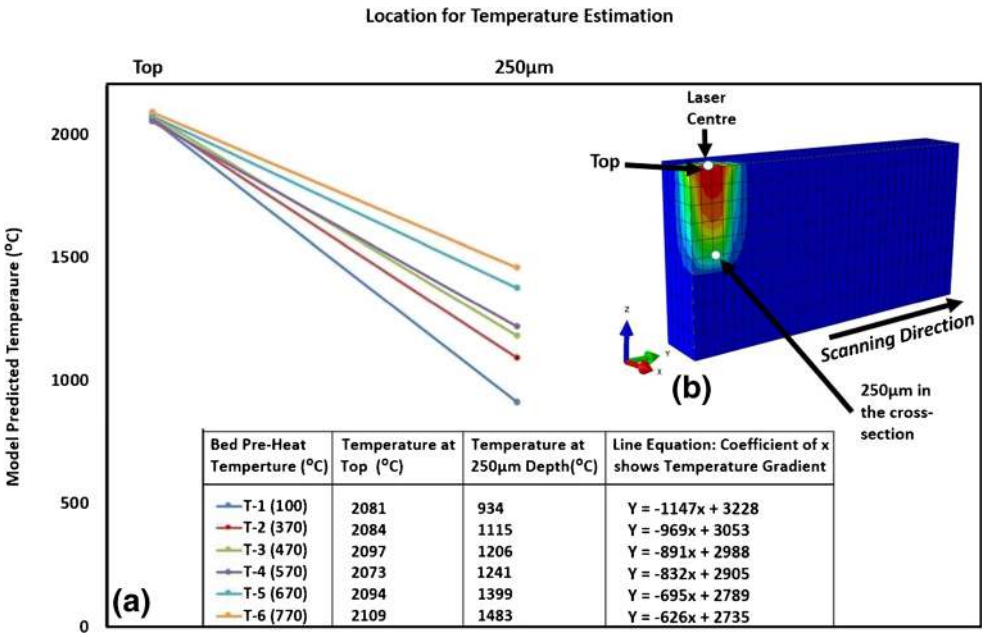

Fig. 7 (a) Temperature gradient prediction between the top surface of the melt-pool and 250-µm depth below the melt-pool from FEA simulation for SLM Ti6Al4V samples, built at different bed pre-heat temperatures. (b) Cross section of the model showing the top and 250-µm position considered for temperature gradient estimation

temperatures of 570 °C. According to the microstructural analysis presented by Ali et al. [12], nano β-particles started forming inside α-laths at pre-heat temperatures of 570 °C. According to refs. [51, 52], α- to β-phase transformation is an endothermic reaction. Therefore, based on the microstructural results of Ali et al. [12], showing the start of nano β-particles inside α-laths could be responsible for the drop in melt-pool peak temperature at 570 °C bed pre-heat temperature.

Figure 8 shows the FEA-predicted cooling rates for SLM Ti6Al4V samples built at different bed pre-heat temperatures along with residual stress (data adapted from the work by Ali et al. [12]). Cooling rate for all test cases were calculated by extracting the time-temperature data (for the heating and cooling cycles from the start to the end of FEA simulation), for the node at the top centre of second laser spot in the FEA simulation. Microsoft Excel was used to calculate the gradient of the cooling curve of the node selected at the top centre of the second laser spot in the FEA simulation. It can be seen from Fig. 8 that both residual stress and cooling rate have an inverse relationship with bed pre-heat temperature. Figure 8 shows a correlation between the trend in cooling rates and residual stress with varying bed pre-heat temperature. Therefore, the FEA model can be used with confidence for

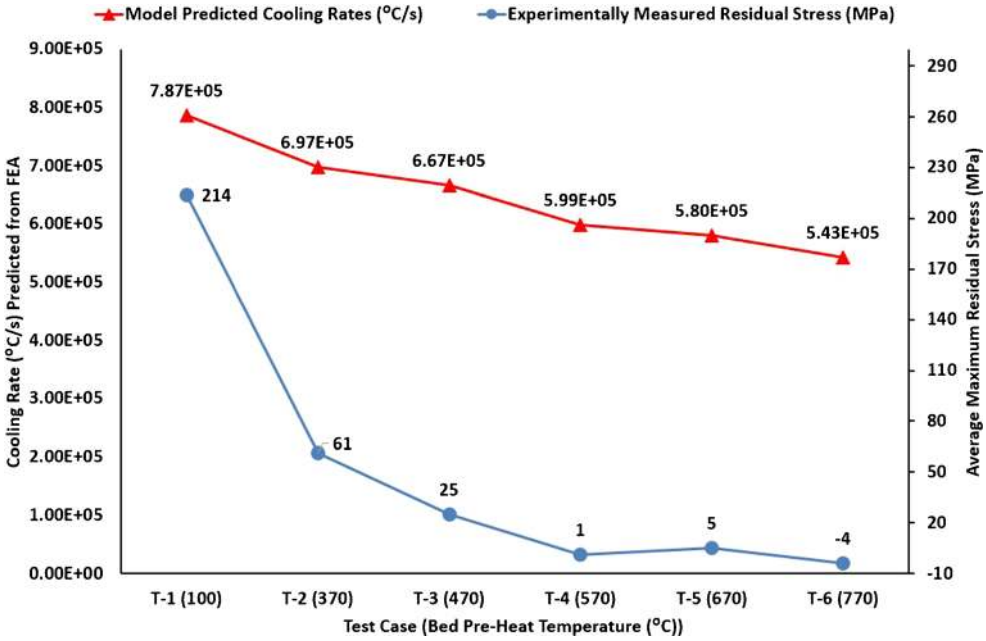

Fig. 8 Cooling rate predicted from FEA simulation for Ti6Al4V SLM samples built at different bed pre-heat temperatures, with residual stress data adapted from ref. [12]

parametric analysis of residual stress in SLM Ti6Al4V components.

4.4 Validation of the effect of FEA-predicted cooling rate on residual stress

SLM Ti6Al4V samples built with process parameters shown in Table 1 based on the density optimisation trials for 75-μm layer thickness resulted in 78-MPa residual stress as shown in Fig. 9a. Keeping the energy density constant at 61.5 J/mm^3 (optimum energy density for achieving nearly fully dense SLM Ti6Al4V parts with 75-μm layer thickness), the required exposure time was calculated for 150-W power using Equation-10. FEA simulation predicted a lower cooling rate for 150-W power and 160-μs exposure time for 75-μm-layer-thickness SLM Ti6Al4V parts. Blocks built with 150-W power and 160-μs exposure time resulted in 55-MPa residual stress as shown in Fig. 9a. The decreasing trend in residual stress correlates with the FEA-predicted trend in cooling rate and thus shows that the FEA simulation is a reliable tool for assessing the effect of SLM parameters on cooling rates and thus residual stress.

FEA simulation was also used to predict the temperature gradient for both sets of parameters used for creating the

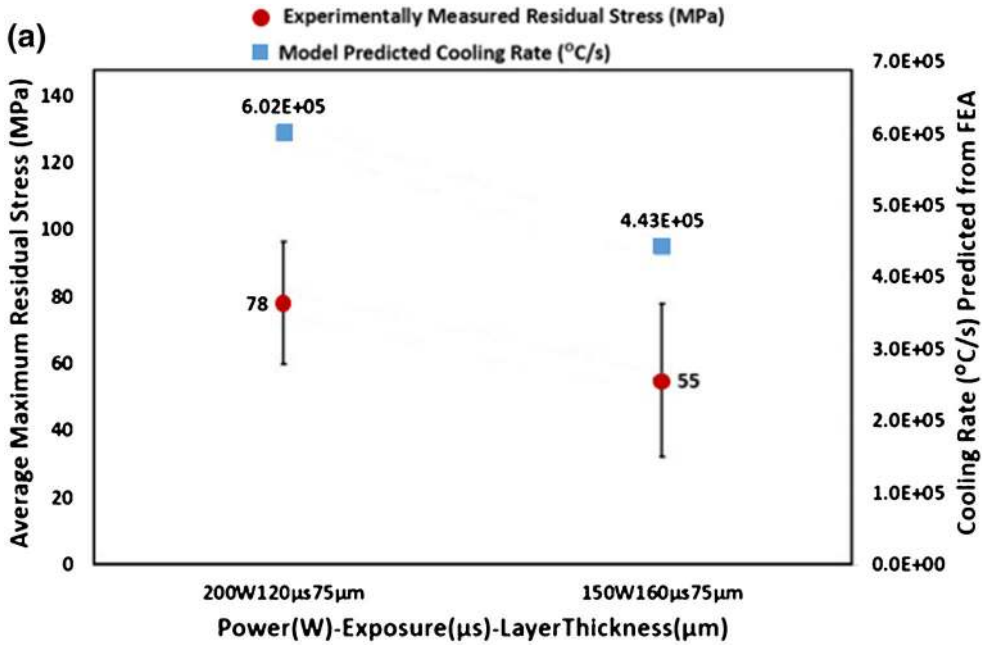

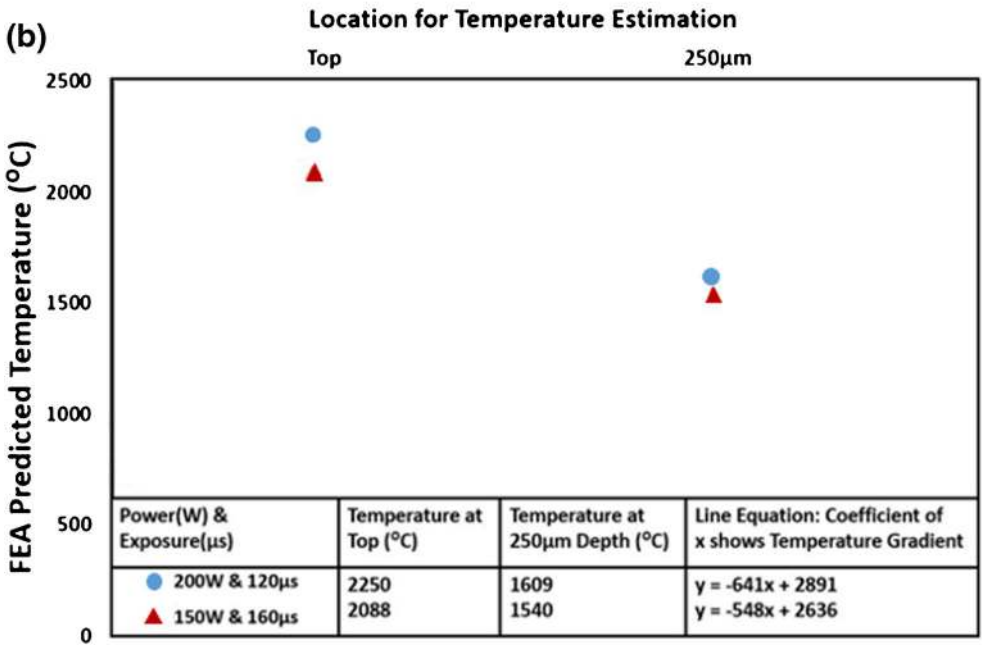

Fig. 9 **a** Effect of power and exposure combination keeping energy density constant on cooling rate and residual stress. **b** Temperature gradient prediction between the top surface of the melt-pool and 250-μm depth below the melt-pool from FEA simulation for SLM Ti6Al4V samples, built with different power and exposure combinations keeping energy density constant at optimum

75-μm-layer-thickness SLM Ti6Al4V samples. Figure 9b shows that the temperature gradient between the top of the melt-pool and 250 μm below the melt-pool top surface is higher for 200-W power and 120-μs exposure combination compared with 150-W power and 160-μs exposure. The decreasing trend in the FEA-predicted temperature gradient according to temperature gradient mechanisms [40, 47] should result in a decreasing trend in residual stress. The decreasing trend in residual shown in Fig. 9a agrees with the decreasing trend in temperature gradients (see Fig. 9b) and therefore increases the confidence in results for the FEA simulation.

Another important observation from Fig. 9b is that the highest temperature in the melt-pool decreases for a lower power of 150 W and higher exposure of 160 μs in combination, compared with a high power of 200 W and lower exposure of 120 μs in combination. This trend in peak temperature with laser power is in agreement with the findings of refs. [44–46], which reported that increase in laser power had a more pronounced effect on the melt-pool peak temperature compared with scan speed (exposure or irradiation time). This further provides as evidence for the validity of the FEA simulation as a tool for analysing the effect of SLM process parameters on residual stress.

5 Conclusions

The developed isotropic enhanced thermal conductivity model for SLM Ti6Al4V treated the laser as a penetrating volumetric heat source and was capable of predicting the melt-pool width (with 14.5% error) and melt-pool depth (with 3% error). The model accurately predicted the temperature evolution along the laser scan path with good correlation to the experimentally determined temperature [44] along the scan path. Accurate prediction of melt-pool dimensions and the trend in temperature evolution along the laser scan path with high correlation to experimental data validates the modelling approach. Therefore, considering enhanced laser penetration to account for heat flow in the melt-pool due to Marangoni convection is a valid approach for modelling the SLM Ti6Al4V melting behaviour. Enhanced penetration depth led to using isotropic enhanced thermal conductivity approach instead of anisotropic enhanced thermal conductivity approach and thus made the FEA model computationally efficient. The model was capable of predicting the start of the solidification region along the laser scan path that was similar to the experimentally determined [44] solidification region. The model accurately predicted the solidification behaviour of the melt-pool; it was then used as a tool for studying the effect of SLM process parameters variation on residual stress.

The trends in model-predicted cooling rates and thermal gradients correlated with the trend in experimentally determined residual stress values. The model accurately predicted the effect of SLM process parameter variation on cooling rates and thermal gradients validated by comparison with the effect of SLM process parameters variation on experimentally determined residual stress. The model clearly showed a reduction in cooling rates and thermal gradients with increasing bed preheat temperature and thus provided evidence for the reduction in residual stress with increasing bed temperature. The effect of bed temperature on peak melt-pool temperature was clearly shown by the model temperature estimates. The model showed a drop in peak melt-pool temperature at a bed preheat temperature of 570 °C, which marks the start of nano β-formation inside α-laths in SLM Ti6Al4V as shown in the work by Ali et al. [12]. The drop in peak melt-pool temperature at 570 °C bed pre-heat temperature is a result of α- to β-phase transformation being an endothermic process. The model accurately predicted the effect of laser power and exposure on peak melt-pool temperature, corroborating the fact that laser power has a stronger effect on peak melt-pool temperature compared with exposure time (scan speed). The model predicted cooling rates and temperature gradients for different power and exposure combinations, showing correlation with the trends in experimentally measured residual stress. The model was helpful in understanding the movement of the solidification front and thus the underlying phenomenon for residual stress build-up.

Correlation of results between the developed model and experiments validate the effectiveness of the two proposed modelling reduction approaches. Using temperature-dependent conductivity of powder Ti6Al4V as a convective heat transfer coefficient to account for heat loss to excess surrounding powder, this reduces the model size as there is no need for modelling excess powder. Similarly, modelling a small substrate and adding a convection boundary condition, using temperature-dependent conductivity of solid Ti6Al4V as convection coefficient accounts for heat loss to the large substrate without the need for modelling a larger substrate. These modelling reduction approaches assisted in reducing the model size and thus improving the computational efficiency of the model.

Acknowledgements The author would like to thank TWI and the EPSRC Future Manufacturing Hub in Manufacture using Advanced Powder Processes (MAPP)(EP/P006566/1) for their support during this investigation.

References

1. Burns M (1993) Automated fabrication: improving productivity in manufacturing. Prentice Hall, Englewood Cliffs
2. Gibson I, Rosen DW, Stucker B (2009) Additive manufacturing technologies: rapid prototyping to direct digital manufacturing. Springer. pp.1–14
3. Casavola C, Campanelli S.L., Pappalettere C (2008) Experimental analysis of residual stresses in the selective laser melting process. In Proceedings of the XIth International Congress and Exposition. Orlando, Florida, USA
4. Kruth J-P, Deckers J, Yasa E, Wauthlé R (2012) Assessing and comparing influencing factors of residual stresses in selective laser melting using a novel analysis method. Proc Inst Mech Eng B J Eng Manuf 226(6):980–991
5. Zaeh MF, Branner G (2010) Investigations on residual stresses and deformations in selective laser melting. Production Engineering : research and development in Germany 4(1)
6. Van Belle LV, Boyer G, Claude J (2013) Investigation of residual stresses induced during the selective laser melting process. Key Eng Mater 554-557:1828–1834
7. Tatsuaki Furumoto TU, Aziz MSA, Hosokawa A, Tanaka R (2010) Study on reduction of residual stress induced during rapid tooling process—influence of heating conditions on residual stress. Key Eng Mater 487-488:785–789
8. Roberts IA (2012) Investigation of residual stresses in the laser melting of metal powders in additive layer manufacturing, University of Wolverhampton. p. 246
9. Joe Elambasseril SF, Bringezu M, Brandt M (2012) Influence of process parameters on selective laser melting of Ti 6Al-4V components, RMIT University School of Aerospace, Mechanical and Manufacturing Engineering (SAMME)
10. Verhaeghe F, Craeghs T, Heulens J, Pandelaers L (2009) A pragmatic model for selective laser melting with evaporation. Acta Mater 57(20):6006–6012
11. Khairallah SA, Anderson A (2014) Mesoscopic simulation model of selective laser melting of stainless steel powder. J Mater Process Technol 214(11):2627–2636
12. Ali H, Ma L, Ghadbeigi H, Mumtaz K (2017) In-situ residual stress reduction, martensitic decomposition and mechanical properties enhancement through high temperature powder bed pre-heating of selective laser melted Ti6Al4V. Mater Sci Eng A 695:211–220
13. Chatterjee AN, Kumar S, Saha P, Mishra PK, Choudhury RA (2003) An experiment design approach to selective laser sintering of low carbon steel. J Mater Process Technol 136:151–157
14. Facchini L, Magalini E, Robotti P, Molinari A, Höges S, Wissenbach K (2010) Ductility of a Ti-6Al-4V alloy produced by selective laser melting of prealloyed powders. Rapid Prototyp J 16(6):450–459
15. Gusarov AV, Pavlov M, Smurov I (2011) Residual stresses at laser surface remelting and additive manufacturing. Phys Procedia 12:248–254
16. Hanzl P, Zetek M, Bakša T, Kroupa T (2015) The influence of processing parameters on the mechanical properties of SLM parts. Procedia Eng 100:1405–1413
17. Fu C, Guo Y (2014) 3-Dimensional finite element modeling of selective laser melting Ti-6Al-4V alloy. in Solid Freeform Fabrication Symposium 2014 Proceedings
18. Safdar S, Pinkerton AJ, Li L, Sheikh MA, Withers PJ (2013) An anisotropic enhanced thermal conductivity approach for modelling laser melt pools for Ni-base super alloys. Appl Math Model 37(3): 1187–1195
19. Dai K, Li XX, Shaw LL (2004) Comparisons between thermal modeling and experiments: effects of substrate preheating. Rapid Prototyp J 10(1):24–34
20. Qian L, Mei J, Wu XH (2007) An experimental and modelling study of laser fabricated samples. Mater Sci Forum Trans Tech Publ 539-543:3637–3642
21. Shiomi M, Yoshidome A, Abe F, Osakada K (1999) Finite element analysis of melting and solidifying processes in laser rapid prototyping of metallic powders. Int J Mach Tools Manuf 39(2): 237–252
22. Matsumoto M, Shiomi M, Osakada K, Abe F (2002) Finite element analysis of single layer forming on metallic powder bed in rapid prototyping by selective laser processing. Int J Mach Tools Manuf 42(1):61–67
23. Katzarov I, Malinov S, Sha W (2002) Finite element modeling of the morphology of β to α phase transformation in Ti-6Al-4V alloy. Metall Mater Trans A 33(4):1027–1040
24. Cheng B, Chou K (2015) Melt pool evolution study in selective laser melting. In 26th Annual International Solid Freeform Fabrication Symposium-An Additive Manufacturing Conference, Austin, TX, USA
25. Fischer P, Karapatis N, Romano V, Glardon R, Weber HP (2002) A model for the interaction of near-infrared laser pulses with metal powders in selective laser sintering. Appl Phys A 74(4):467–474
26. Gusarov AV, Smurov I (2010) Modeling the interaction of laser radiation with powder bed at selective laser melting. Phys Procedia 5:381–394
27. Antony K, Arivazhagan N, Senthilkumaran K (2014) Numerical and experimental investigations on laser melting of stainless steel 316L metal powders. J Manuf Process 16(3):345–355
28. Song B, Dong S, Liao H, Coddet C (2012) Process parameter selection for selective laser melting of Ti6Al4V based on temperature distribution simulation and experimental sintering. Int J Adv Manuf Technol 61(9):967–974
29. Polivnikova T (2015) Study and modelling of the melt pool dynamics during selective laser sintering and melting, EPFL
30. Dai K, Shaw L (2004) Thermal and mechanical finite element modeling of laser forming from metal and ceramic powders. Acta Mater 52(1):69–80
31. Papadakis L, Loizou A, Risse J, Bremen S (2013) A thermo-mechanical modeling reduction approach for calculating shape distortion in SLM manufacturing for aero engine components. Proceedings of the 6th International Conference on Advanced Research in Virtual and Rapid Prototyping, Leiria. pp. 1–5
32. Roberts IA, Wang CJ, Esterlein R, Stanford M, Mynors DJ (2009) A three-dimensional finite element analysis of the temperature field during laser melting of metal powders in additive layer manufacturing. Int J Mach Tools Manuf 49(12–13):916–923
33. Gusarov AV, Smurov I (2009) Two-dimensional numerical modelling of radiation transfer in powder beds at selective laser melting. Appl Surf Sci 255(10):5595–5599
34. Lopez-Botello O, Martinez-Hernandez U, Ramírez J, Pinna C, Mumtaz K (2017) Two-dimensional simulation of grain structure growth within selective laser melted AA-2024. Mater Des 113: 369–376
35. Parry L, Ashcroft IA, Wildman RD (2016) Understanding the effect of laser scan strategy on residual stress in selective laser melting through thermo-mechanical simulation. Addit Manuf 12(Part A):1–15
36. Mills K et al (1998) Marangoni effects in welding. Philosophical Transactions-Royal Society of London Series A Mathematical Physical and Engineering Sciences, p. 911–926
37. Yuan P, Gu D D (2015) Molten pool behaviour and its physical mechanism during selective laser melting of TiC/AlSi10Mg nanocomposites: simulation and experiments. J Phys D Appl Phys 48(3): 035303
38. Cheng B, Shrestha S, Chou K (2016) Stress and deformation evaluations of scanning strategy effect in selective laser melting. Addit Manuf 12(Part B):240–251

39. Donachie MJ (2000) Titanium: a technical guide, 2nd Edition. ASM International
40. Shi Y, Shen H, Yao Z, Hu J (2007) Temperature gradient mechanism in laser forming of thin plates. Opt Laser Technol 39(4):858–863
41. Tolochko NK, Khlopkov YV, Mozzharov SE, Ignatiev MB, Laoui T, Titov VI (2000) Absorptance of powder materials suitable for laser sintering. Rapid Prototyp J 6(3):155–161
42. Vasinonta A, Beuth JL, Griffith M (2006) Process maps for predicting residual stress and melt pool size in the laser-based fabrication of thin-walled structures. J Manuf Sci Eng 129(1):101–109
43. Simchi A (2006) Direct laser sintering of metal powders: mechanism, kinetics and microstructural features. Mater Sci Eng A 428(1):148–158
44. Yadroitsev I, Krakhmalev P, Yadroitsava I (2014) Selective laser melting of Ti6Al4V alloy for biomedical applications: temperature monitoring and microstructural evolution. J Alloys Compd 583: 404–409
45. Alimardani M, Toyserkani E, Huissoon JP, Paul CP (2009) On the delamination and crack formation in a thin wall fabricated using laser solid freeform fabrication process: an experimental–numerical investigation. Opt Lasers Eng 47(11):1160–1168
46. Manvatkar V, De A, DebRoy T (2015) Spatial variation of melt pool geometry, peak temperature and solidification parameters during laser assisted additive manufacturing process. Mater Sci Technol 31(8):924–930
47. Mercelis P (2007) Control of selective laser sintering and selective laser melting processes. KU Leuven, Leuven, Belgium
48. Shiomi M, Osakada K, Nakamura K, Yamashita T, Abe F (2004) Residual stress within metallic model made by selective laser melting process. CIRP Ann Manuf Technol 53(1):195–198
49. Vora P, Mumtaz K, Todd I, Hopkinson N (2015) AlSi12 in-situ alloy formation and residual stress reduction using anchorless selective laser melting. Addit Manuf 7:12–19
50. Vrancken B et al (2015) Influence of preheating and oxygen content on selective laser melting of Ti6Al4V. In Proceedings of the 16th RAPDASA Conference. RAPDASA, Annual International Conference on Rapid Product Development Association of South Africa 4–6 November 2015. Pretoria, South Africa
51. Sha W, Malinov S (2009) Titanium alloys: modelling of microstructure, properties and applications. Elsevier
52. Homporova P et al (2011) Dynamic phase evolution in titanium alloy Ti-6Al-4V. in Proc. 12th World Conference on Titanium